

# Real time atomic scale imaging of nanostructural evolution in aluminium alloys

## Supporting Information

*Sairam K. Malladi<sup>†,‡</sup>, Qiang Xu<sup>‡</sup>, Marijn A. van Huis<sup>‡,§</sup>, Frans D. Tichelaar<sup>‡</sup>,  
K. Joost Batenburg<sup>††,‡‡</sup>, Emrah Yücelen<sup>‡,§§</sup>, Beata Dubiel<sup>†††</sup>, Aleksandra Czyska-  
Filemonowicz<sup>†††</sup>, Henny W. Zandbergen<sup>†\*</sup>*

### **Contents:**

1. More details on heat treatment experiments on AA 2024
2. Details on discrete tomography
3. Analysis of growth kinetics from experimental *in situ* precipitation data
4. Analysis of the HR-STEM images of the precipitates
5. Experimental limitations
6. STEM movie analysis using FIJI/ImageJ
7. List of movies and captions
8. Table on diffusion coefficients (Supplementary Table S1)

## 1. More details on heat-treatment experiments on AA 2024

The initial heat-treatment experiments are performed by heating the specimen from room temperature upwards in steps of 20°C per minute and recording the images in bright-field (BF) TEM mode. The microstructure at room temperature consists of precipitates measuring 50(±20) nm × 50(±20) nm × 200 (±20) nm in the matrix and randomly shaped precipitates with sizes ranging from 0.3 to 1.5 μm. Most of these matrix precipitates have been identified from their composition measured with EDX as Al<sub>20</sub>Mn<sub>2</sub>Cu<sub>3</sub> type, whereas the grain-boundary precipitates are θ-type (Al<sub>2</sub>Cu) or, in a few cases, S-phase type (Al<sub>2</sub>CuMg) precipitates. On heating from room temperature to ~180°C, the microstructure remains the same. From 180°C onwards, significant changes in the size of grain-boundary precipitates are observed. Heating between 220°C and 280°C, results in the formation of lath-like nano-precipitates. These lath-like precipitates are more evident in ADF-STEM mode (Figure S2). Therefore, we decided to conduct heat-treatment experiments while imaging in STEM mode.

Figure S3 shows STEM-ADF images acquired at various stages while being heated from 120 to 360°C. The temperature is increased in steps of 30°C and at every stage the specimen is held at the set temperature first for ~1 min to observe any changes occurring at this temperature and then for ~5 min to obtain the EDX maps. The heating profile is shown at the bottom right corner in Figure S3. The corresponding qualitative elemental maps are shown in Figure S4. From the heat-treatment and compositional analysis, it is observed that from room temperature to ~180°C, the microstructure of 2024-T3 alloy remains unchanged and is largely dominated by plate-type precipitates enriched in Cu and Mn as shown in the first row (100°C) of Figure S4. Heating from 180°C upwards results in redistribution of Cu, indicated by a stronger Cu signal from the nodular features formed at the edge of the specimen. Moreover a change in the size of the grain-boundary

precipitates enriched in Cu is also observed. From 220°C upwards, the formation of lath-like nanoprecipitates is observed. These precipitates are allowed to grow until 270°C and are mapped at a higher magnification at 270°C (peak-aged condition). The nanoprecipitates are identified as Cu and Mg containing S-phase type precipitates. Heating beyond 300°C causes these precipitates to dissolve. At 330°C, the nanoprecipitates dissolve completely into the matrix, whereupon the Cu-rich grain-boundary precipitates start to shrink. Heating gradually from 330 to 410°C causes most of the Cu to dissolve from the precipitates to the matrix. Throughout the heating process, Mn-rich precipitates remain intact. The temperature range (250–300°C) as well as the time range (a few minutes) for the precipitation of nanoprecipitates is in agreement with the previously observed values by Thomas & Whelan in model Al-Cu alloy, whereas studies on Al-Cu-Mg alloys have shown that the precipitation of large densities of S-phase-type precipitates is enhanced above 200°C. One such study using differential scanning calorimetry (DSC) shows the dominant exothermic heat effect between about 220°C and 280°C, which is associated with the formation of S-phase-type precipitates<sup>1</sup>.

Figure S5 shows the STEM-ADF images and the corresponding quantified elemental maps for Cu, Mg obtained at 200°C and 250°C from another specimen. In the region marked by the square in Figure S5a, approximately ~3.4 at% Cu and ~2 at% Mg is detected at 200°C, whereas after formation of the lath-like precipitates at 250°C, Figure S5e, the matrix shows ~1.5 at% Cu and ~1.7% Mg. Most of the precipitates show ~10 at% Cu and ~9 at% Mg, and it is known that S-type precipitates have a Cu/Mg ratio close to 1. As the accuracy of determining the composition from EDX is within  $\pm 1\%$  and in this temperature range it is expected that S-type intermediate precipitates form in these alloys, they are identified as S-type precipitates. The most notable

compositional change from this EDX study is the decrease in matrix Cu content from 3.4 at% to 1.5 at% before and after precipitation.

## **2. Details on discrete tomography**

The images obtained in a TEM are essentially two-dimensional (2D) projections of the cross section on which the electron beam is incident. In order to obtain three-dimensional (3D) information from a TEM specimen, it is necessary to perform tomography where the specimen is tilted over a large angular range and projections are obtained at each of the intermediate steps. For conventional reconstruction methods such as back projection schemes and the simultaneous iterative reconstructive technique (SIRT), it is preferable to have more than 100 projections, tilting the sample in steps of 1–2° over a range of at least  $\pm 60^\circ$ . However, in this study, we have employed the discrete algebraic reconstruction technique (DART)<sup>2</sup> from STEM-ADF images acquired in steps of 1° over a range of  $\pm 45^\circ$ .

The DART method is based on the assumption that a 3D reconstruction of the specimen should contain only one grey level for each of the compositions in the specimen, which is very much valid for the precipitates of a particular morphology at a given temperature. Taking advantage of this property, the DART algorithm operates by applying a sequence of alternating reconstruction and segmentation steps. Each reconstruction step operates only on the boundary of the features (precipitates in this case), which is identified by thresholding the reconstruction from the previous step. Figure S6 shows a comparison of slices from SIRT and DART reconstruction methods respectively. By using this method, either the quality of the reconstruction can be improved significantly, or the number of required projection images can be reduced as shown in Figure S6.

Although the discrete tomography technique is capable of accurate reconstruction from a limited angular range, the relatively small range from  $-45$  to  $+45$  degrees used in these experiments can still introduce some elongation effects of the precipitates perpendicular to the viewing direction, which can be observed in Figure 2g. For the reconstructions in this study, the surface of the sample is determined by selecting the termination points of the precipitates that extend the most to each side and the distance between these points corresponds to the specimen thickness. Owing to blurring effects at the boundaries of the precipitates, we estimate that these points are determined within an accuracy of 5 voxels, corresponding to a length of 5 nm for the first dataset (Figure 1 and Supplementary Movie S2) and 3 nm for the second data set (Figure 2 and Supplementary Movie S5). A more accurate determination of the surface could be done by using markers as is commonly done in life science TEM tomography.

### **3. Analysis of growth kinetics from experimental *in situ* precipitation data**

Figure 2d and Supporting Supplementary Movie S3 allow extracting detailed, time-resolved information on the growth kinetics. The precipitates that are formed at dislocations nucleate earlier in time but show the same growth characteristics as precipitates that are formed free in the matrix. Figure S7a shows the average width and length as a function of  $t^{1/2}$  (after synchronizing the nucleation moments to  $t=0$ ). The width remains nearly constant, showing that growth in the lateral dimensions is interface limited. There is one-dimensional growth in the length direction.

From Figure S7 it is clear that the average length increases linearly with the square root of time, corresponding to classical volume diffusion controlled growth. The half-length is commonly expressed<sup>3</sup>:

$$\frac{1}{2}L(t) = 2(\beta D)^{1/2}t^{1/2}$$

Where  $\beta$  is the dimensionless growth parameter, and  $D$  is the diffusivity of the slowest diffusing element (Cu,  $D_{\text{Cu}} = 4.0 \cdot 10^{-19} \text{ m}^2\text{s}^{-1}$  at a temperature of 225 °C). The growth parameter can be derived from the slope  $dL/d(t^{1/2}) = 4(\beta D)^{1/2}$  of the linear fit for the average precipitate dimensions and is displayed in Figure S7b. The growth rate is lower at longer annealing times, which may be caused by a lower level of supersaturation after precipitation, or by the limited thickness of the slab (140 nm). At shorter annealing times, the growth rate is also lower. Figure 3 reveals unique additional information on the growth process which cannot be obtained with any other experimental method: the precipitation process consists of more than just atomic diffusion, as in the early stages atomic clusters coalesce with the S-type precipitates thereby contributing to their growth. Until now, in TEM studies, average dimensions of precipitates that have nucleated at different moments in time are considered. However with the current methodology, time-resolved information is obtained from individual precipitates, which allows separating nucleation and growth, so that much more reliable values for the growth parameter  $\beta$  are obtained. The present findings call for more advanced growth models, taking into account not only nucleation and growth of precipitates, but also the coalescence with precursor, GP zones. The detailed experimental information obtained using the current methodology will be required for developing and validating such advanced models.

#### **4. Analysis of the HR-STEM images of the precipitates**

The STEM images in Figure 3 and Supplementary Movie S6 are rather fuzzy compared to STEM images reported in the literature<sup>4</sup>, because our specimen thickness (150 nm) is optimized to follow the evolution of the precipitates and not to achieve the best resolution, which requires a thickness of no more than 50 nm. Nevertheless, it is clear from our STEM images that there are strings of bright dots 4.5 Å apart along the [210] direction (see Figure 3), which fit well with the

Al lattice. The fact that these dots are bright suggests that they are Cu or Cu-rich columns. The S phase has this specific feature of the Cu (210)<sub>Al</sub> planes, where in the neighbouring (210) plane Al is replaced by Mg (Mg is larger than Al and Cu smaller than Al, compensating largely each other's volume change), thus forming a Cu-Mg slab. The distance between the slabs can vary according to the literature. A sequence of slab–slab distances is shown in Figure S8, leading to compositions of CuMgAl<sub>n</sub>. The distance as well as the relative positions of the bright dots in the STEM image fit well with the model for CuMgAl<sub>5</sub>. The precipitates are clearly not single crystalline; there are bands without a clear presence of the CuMg slabs. These are likely due to antiphase boundaries.

## 5. Experimental limitations

While carrying out the *in situ* TEM experiments, it is important to know the limitations and select a suitable window for experiments for proper interpretation of the results. This is because the TEM specimens have a large surface-to-volume ratio and thus some of the constraints of the surrounding material found in bulk specimens are absent. In this section, we describe the experimental constraints related to heating and beam damage encountered during our experiments.

### *a. Thermal grooving*

When the Al alloy specimens are heated for longer than 30 min at temperatures higher than 400°C, we observed in STEM mode the formation of a dark zone close to the grain boundary (Figure S9a). These are regions depleted of Al, as shown by the elemental map (Figure S9b). This depletion, called grain boundary grooving, is caused by atoms moving away from the intersection of a grain boundary and the free surface, such that the contact angles between the

free surfaces of the two grains and the grain boundary obtain an equilibrium value dictated by the respective surface energies. The atom movements are made possible by surface diffusion at higher temperature. Thermal grooving can be avoided by performing the solution heat treatment at 400°C for short durations (usually less than 10 min).

*b. Surface diffusion at specimen edges*

Heating at temperatures higher than 450°C also results in surface diffusion from the edges of the specimen as shown in Figure S10. The temperature at which this surface diffusion starts varies from specimen to specimen but it is usually observed to start from thinner regions of the specimen close to the edge. Once this takes place, the specimen becomes unusable for further quenching and aging experiments.

*c. Electron beam damage*

Electron beam-induced damage is a very well-known problem in TEM. To minimize the beam damage while enhancing contrast, all our experiments are performed in STEM mode, whereby the short dwell time of the beam minimizes beam damage. However, while acquiring the EDX maps, we tried several combinations to maximize the signal for EDX mapping. The EDX maps are obtained using a probe-corrected FEI TITAN<sup>3</sup> 60-300 equipped with ChemiSTEM™ technology (X-FEG, and Super-X detection system). All the maps presented here have a frame size of 512×512 pixels<sup>2</sup> with a frame time of 100 s, averaged over three frames, and a probe current of ~0.3 nA, making the effective acquisition time 5 min. In order to accelerate the EDX acquisition, we tried increasing the probe current by a factor of 10 by changing the spot size. However, this resulted in severe beam damage. Figure S11 shows a comparison of an image obtained using probe currents of ~0.3 and ~3 nA respectively. Attempts to obtain EDX maps

using a probe current of  $\sim 3$  nA haven't been successful due to the beam damage (formation of holes in the specimen).

## 6. STEM movie analysis using FIJI/ImageJ

Figure S12a shows an STEM image acquired from the end of the Supplementary Movie S3. In this section, we describe the process used to acquire the length of one of the precipitates marked 1 in Figure S12a. In order to enhance the contrast of the edges of the precipitate, the image stack is first duplicated and processed using a Gaussian blur (sigma radius 2.00). Then the original image stack is divided by the processed image stack to produce a stack of images with sharp precipitate edges. Next, the image stack is aligned to make the precipitate of interest vertical as shown in Figure S12b, is a snapshot of the end of such an image stack. This is done because the rest of the procedure is conducted straightforwardly with the existing plug-ins. Subsequently, the precipitate of interest is isolated and the orthogonal views of this precipitate are generated. Figure S12c is an YZ projection of an image stack of precipitate 1 in Figure S12a. The pixels along the horizontal axis of this image correspond to each frame from the image stack, which in turn represents the time. The pixels along the vertical direction correspond to the change in the length of the precipitate along the vertical axis from each of the frames of the image stack. To determine the length of the precipitate, first a bare outline map, Figure S12d, is extracted from the 'Analyze Particles' plugin for ImageJ<sup>5</sup> after selecting the appropriate threshold level. All the pixels outside the outline are set to 0 and the pixels inside the outline are set to 1 to generate a bitmap image as shown in Figure S12e. The length of the precipitates is then calculated by adding the pixels along the vertical axis and multiplying with the pixel size from the STEM images.

## 7. List of movies and captions

**Supplementary Movie S1:** Aligned STEM-ADF movie showing tilt series of 91 STEM-ADF images acquired between  $-45^\circ$  to  $+45^\circ$  from a specimen heated at  $250^\circ\text{C}$  for approximately 2 minutes. The angle corresponding to the projection is shown at the top left corner of the movie. In this movie, the tilt axis is along the central vertical of the images.

**Supplementary Movie S2:** Reconstructed tomogram from STEM-ADF tilt-series shown in Supplementary Movie S1. In this movie, the tomogram is rotated by  $360^\circ$  about the vertical tilt axis at the centre of the reconstructed volume.

**Supplementary Movie S3:** STEM-ADF movie showing the growth of precipitates in a FIB specimen of AA2024 heated at  $225^\circ\text{C}$ . The time (in seconds) for which the specimen is held at this temperature from the moment it is set at  $225^\circ\text{C}$  is shown on the top left corner.

**Supplementary Movie S4:** Aligned STEM-ADF movie showing tilt series of 91 STEM-ADF images acquired between  $-45^\circ$  to  $+45^\circ$  from the specimen after heating at  $225^\circ\text{C}$  for 840 s (Supplementary Movie S3). The angle corresponding to the projection is shown at the top left corner of the movie. In this movie, the tilt axis is along the central vertical of the images.

**Supplementary Movie S5:** Reconstructed tomogram from STEM-ADF tilt-series shown in movie S4. In this movie, the tomogram is rotated by  $360^\circ$  about the vertical tilt axis at the centre of the reconstructed volume. At specific orientations, each of the three families of precipitates that have grown along the  $\{100\}_{Al}$ , i.e. precipitates along the dislocations at the middle of the foil, two families of precipitates relatively parallel to the surface are evident.

**Supplementary Movie S6:** HR-STEM movie of a FIB specimen of AA2024 heated at 200°C showing the growth of one of the precipitates as well as the dissolution of two of the atom clusters. The acquisition of the movie starts approximately 10 minutes after the temperature is set to 200°C at the rate of 2 minutes per frame. The initial 10 minutes are spent locating the appropriate region as well as making the necessary alignments for carrying out the HR-STEM studies.

**Supplementary Movie S7:** STEM-ADF movie showing the growth of precipitates in a FIB specimen of AA2024 heated at 250°C. The time for which the specimen is held at this temperature from the moment it is set at 250°C is shown next to the scale bar. After the acquisition of the movie stopped, the EDX maps from this region were obtained (Figure 4).

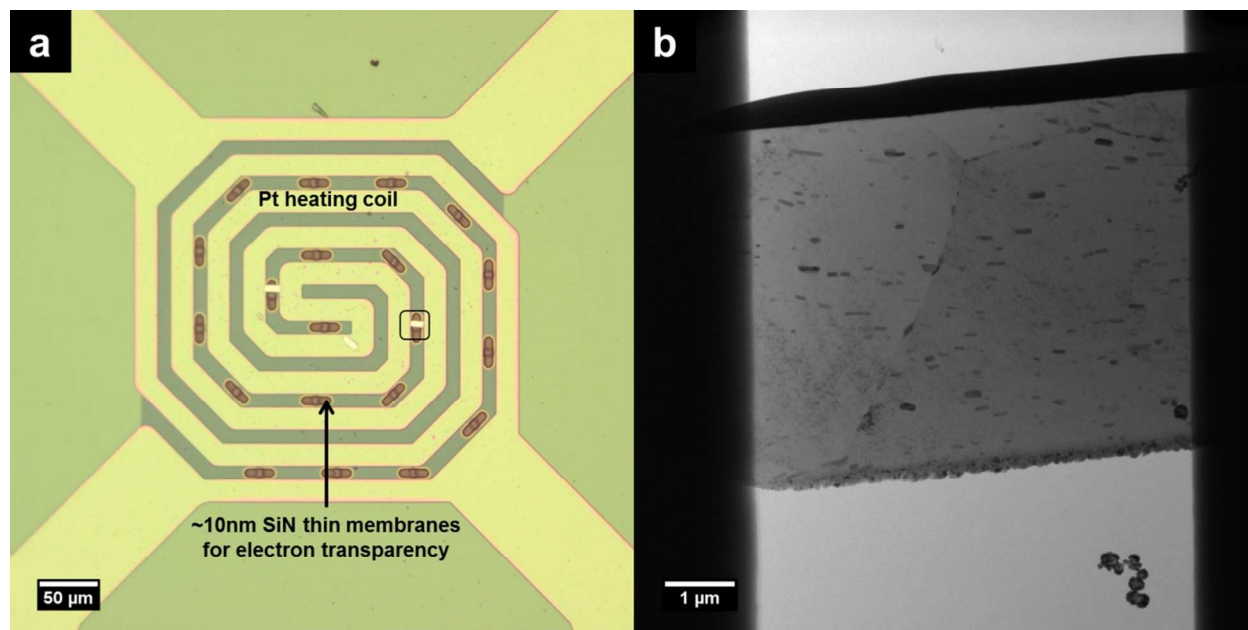


**Figure S1. (a)** Optical micrograph showing FIB lamellae on thin membranes of a MEMS based heating chip; **(b)** Bright-field TEM image of FIB lamellae indicated by the square in (A).

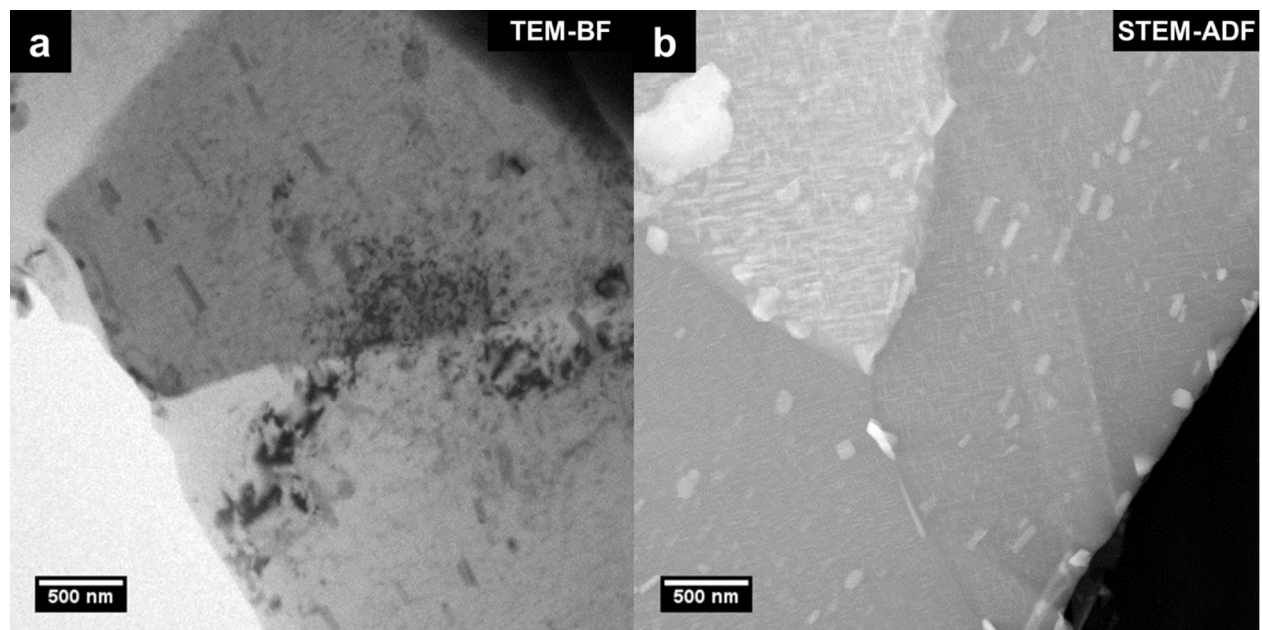


**Figure S2.** Comparison of two images acquired from two different specimens in (a) BF-TEM and (b) STEM-ADF at 240°C. The lath-like S-phase type precipitates are better visible in STEM mode than in conventional BF-TEM mode.

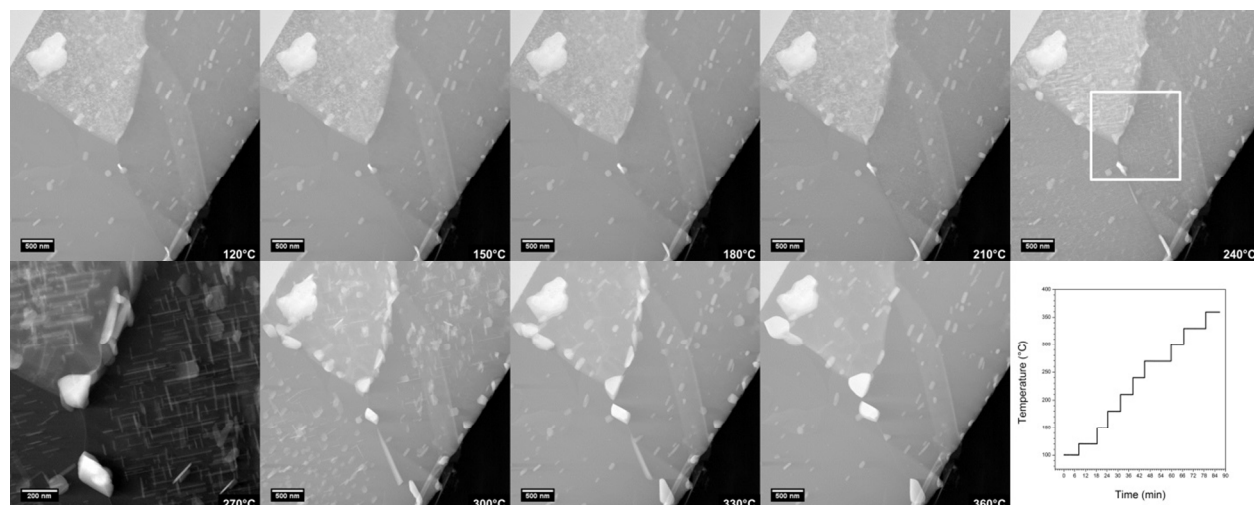


**Figure S3.** STEM-ADF images acquired after heating the AA2024 FIB specimen at the mentioned temperatures using the heating profile shown on the bottom right corner. Notice the changes in the size of the grain-boundary precipitates. A higher magnification image of the area marked by the square in the image at 240°C is shown at 270°C to highlight the formation of lath-like nanoprecipitates in the matrix. Also, the presence of a precipitate-free zone close to the grain boundary is evident. The lath-like precipitates tend to dissolve back into the matrix beyond 300°C.

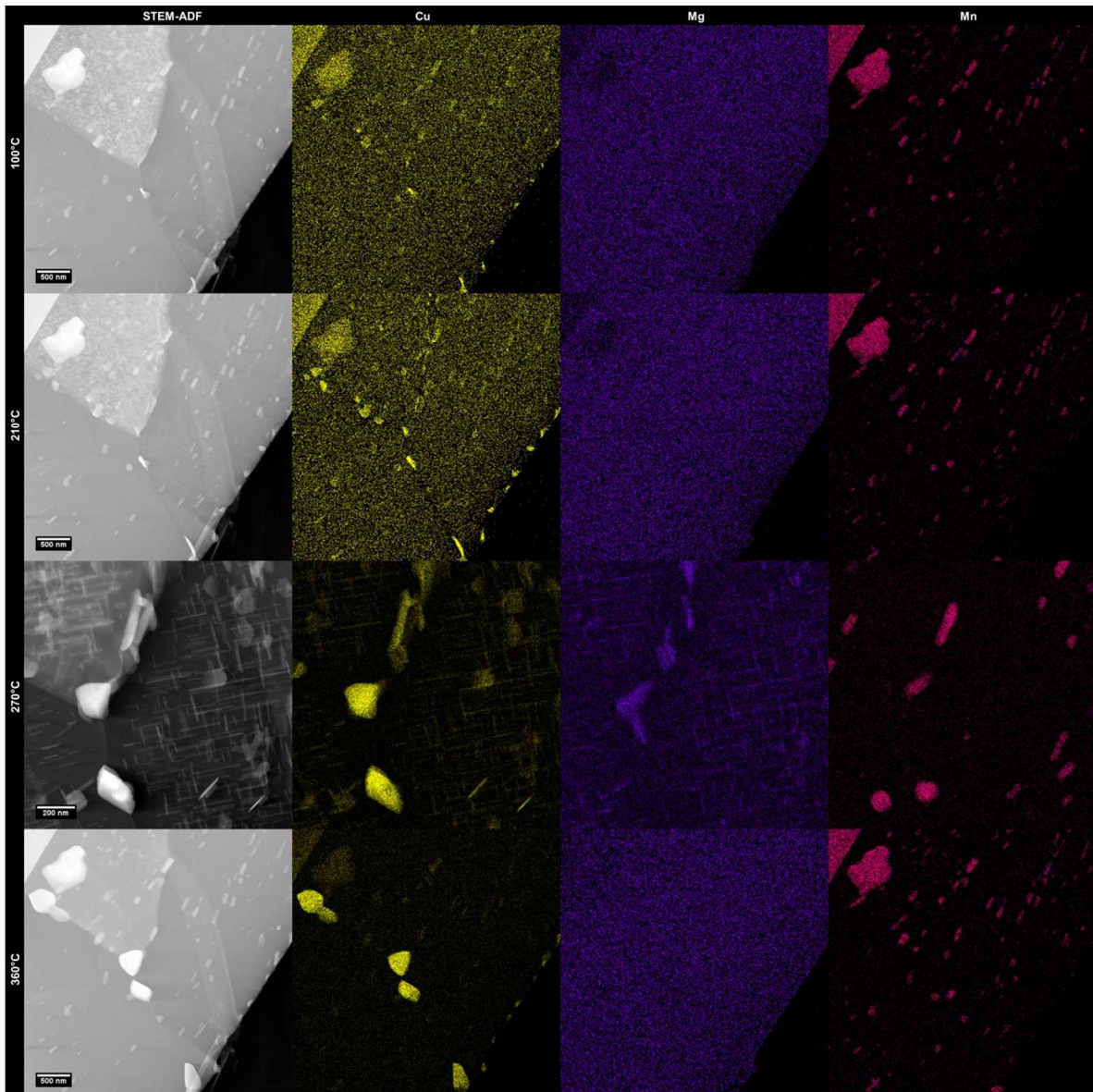


**Figure S4.** Qualitative EDX maps obtained at each of the intermediate stages of heat-treatment shown in Figure S3. These maps are obtained with a frame size of  $512 \times 512$  pixels<sup>2</sup> and a frame time of 100 s, averaged over three frames. Notice the Cu redistribution associated with the precipitation at grain boundaries and precipitation in the matrix during the heat-treatment processes. The lath-like nanoprecipitates are enriched with Cu and Mg, suggesting S-phase-type compositions. Throughout the heat-treatment process, the Mn-rich precipitates remained as they are at room temperature.

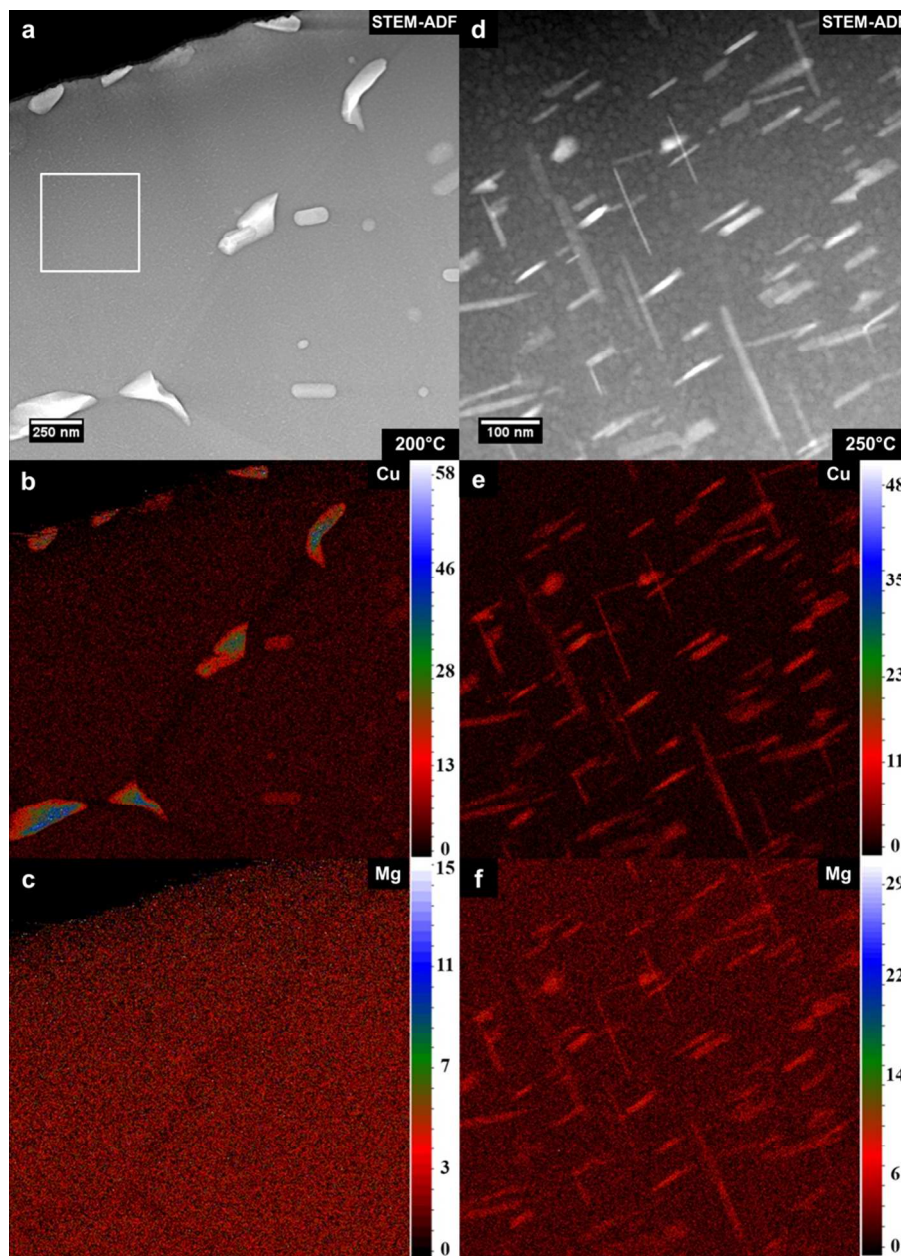


**Figure S5.** STEM-ADF and corresponding quantitative EDX maps obtained at (a-c) 200°C and (d-f) 250°C. The maps at 250°C obtained from the region marked by the square in (a) show a decrease in matrix Cu content from ~4 at.% to ~1 at.%, whereas the lath-like precipitates are enriched with ~20 at.% Cu. A similar trend is observed in case of the Mg: they show a decrease in matrix Mg content from ~3 at.% to 1 at.% while the precipitates are enriched with ~8 at.% Mg.

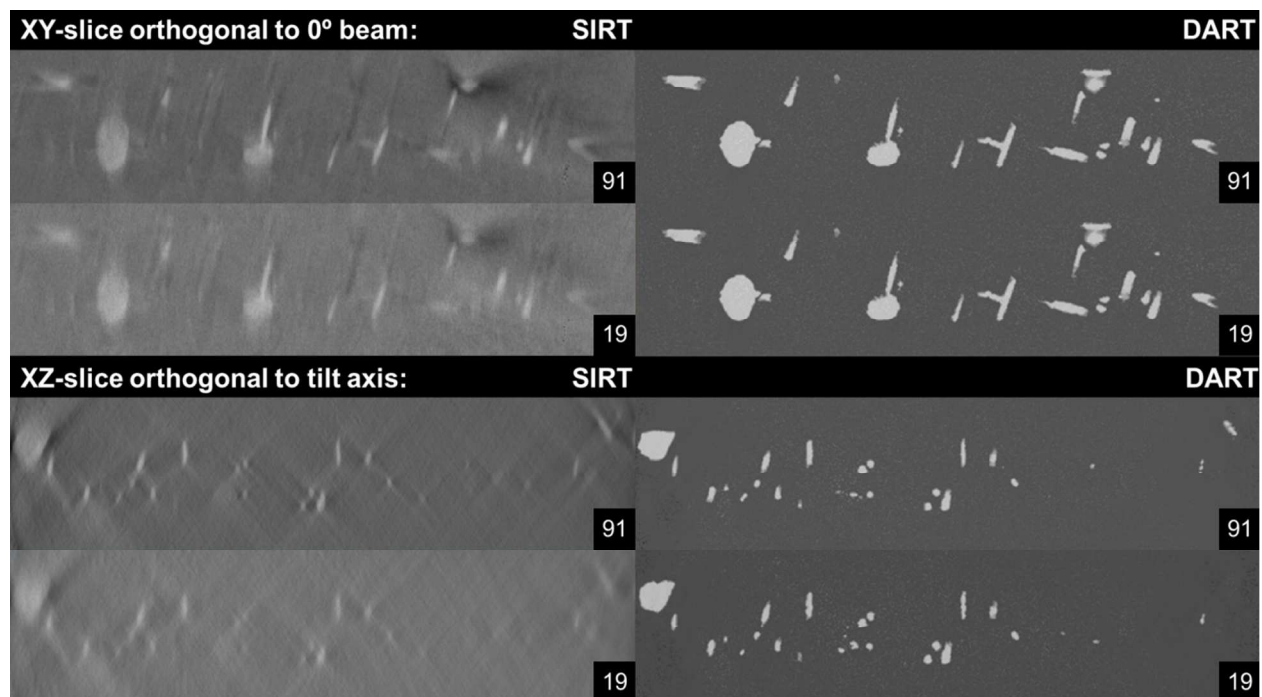


**Figure S6.** Comparison between the reconstructions based on SIRT and DART algorithms using 91 (1° step) and 19 projections (5° step) from STEM-ADF images obtained within a tilt range of  $\pm 45^\circ$ .

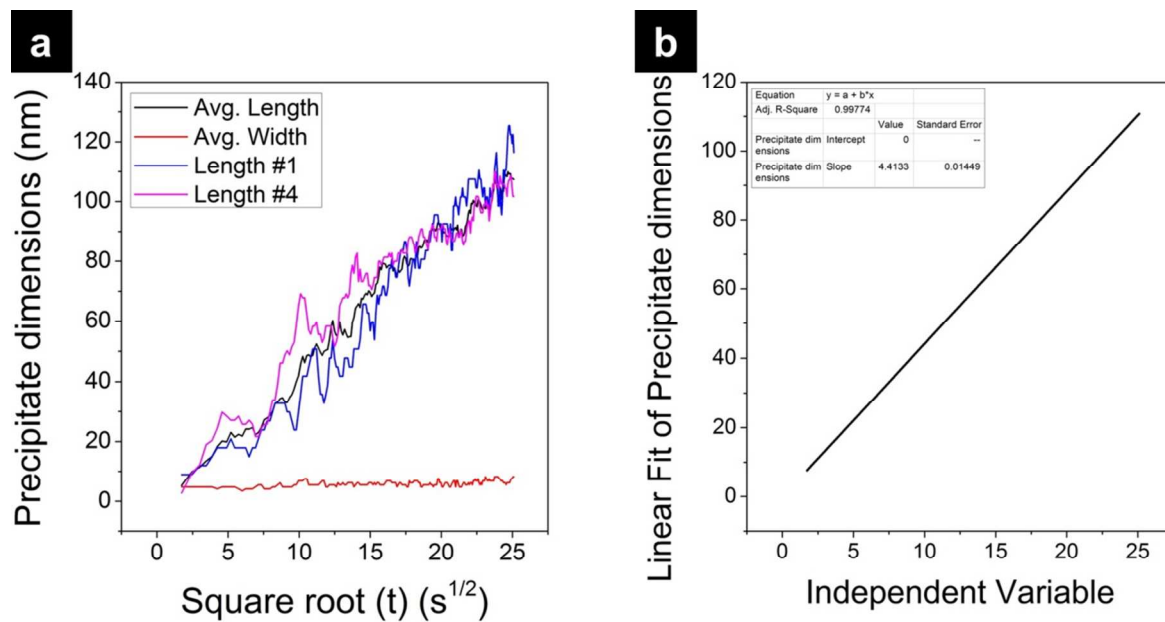


**Figure S7: (a)** Precipitate dimensions monitored from the moment of nucleation, as a function of  $t^{1/2}$ . **(b)** Growth parameter  $\beta = 3.04$ , derived from the slope of the linear fit from the average precipitate length in **(a)**.

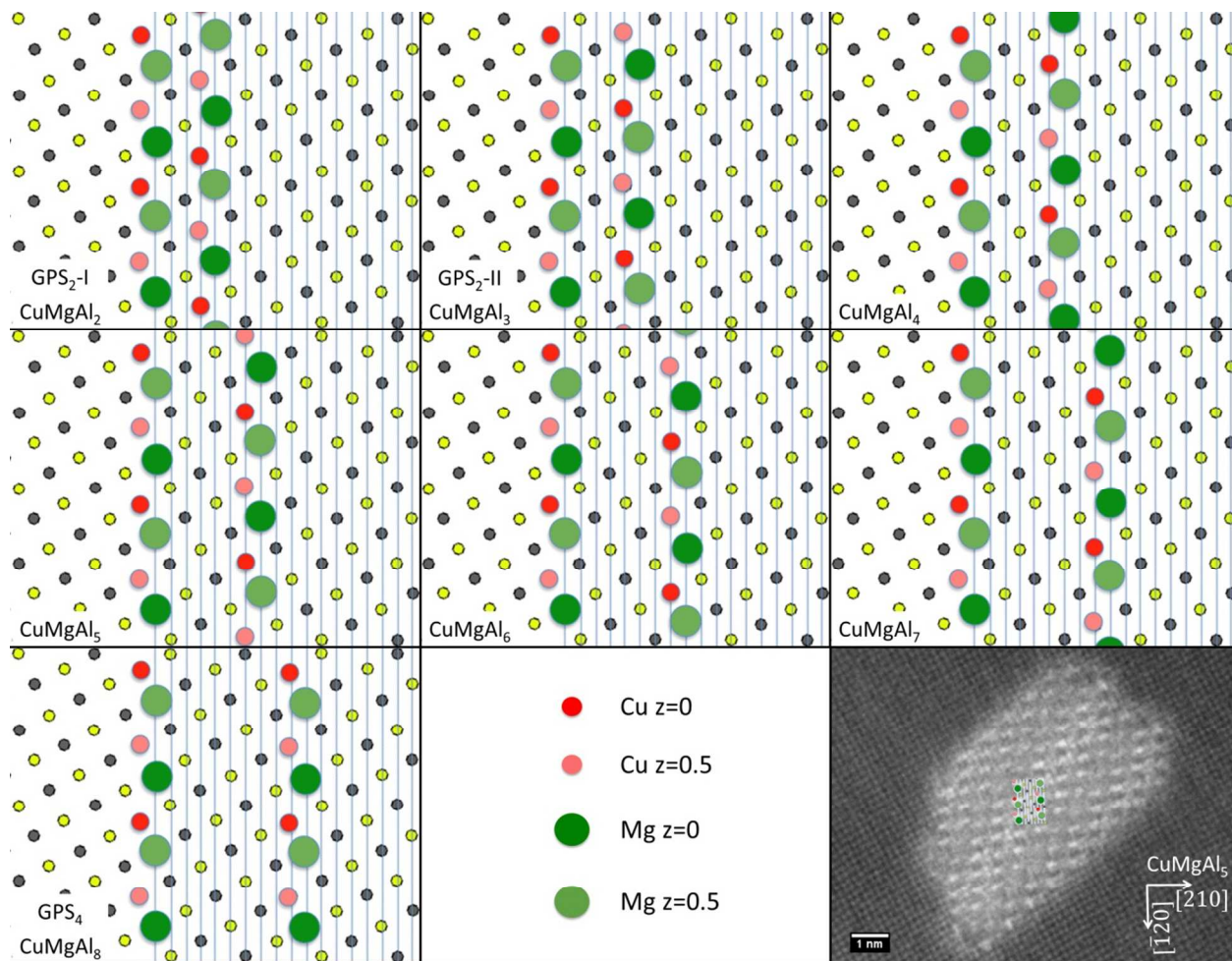


**Figure S8.** Sequence of slab-slab distances leading to compositions  $\text{CuMgAl}_n$  during the growth of S-type intermediate precipitates in AA2024. The compositions previously identified as GPS-type are also mentioned here. The heights of the Cu and Mg atoms refer to the positions in the Al lattice. For precipitate 1 in Figure 3, the distance as well as the relative positions of the bright dots in the STEM image fit well with the model for  $\text{CuMgAl}_5$ , as shown by the overlay in the image at the bottom right corner.

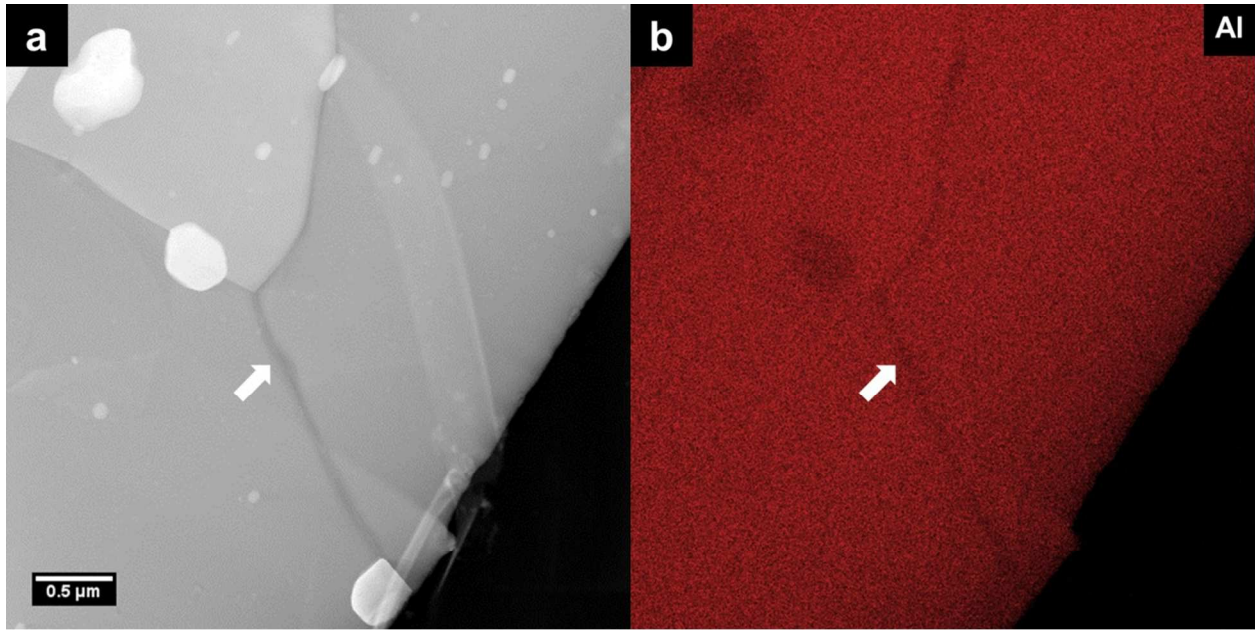


**Figure S9.** (a) STEM-ADF and the corresponding elemental map (b) showing the thermal-grooving at the grain boundary after holding an AA2024 specimen at temperatures higher than 400°C for longer than 30 min.

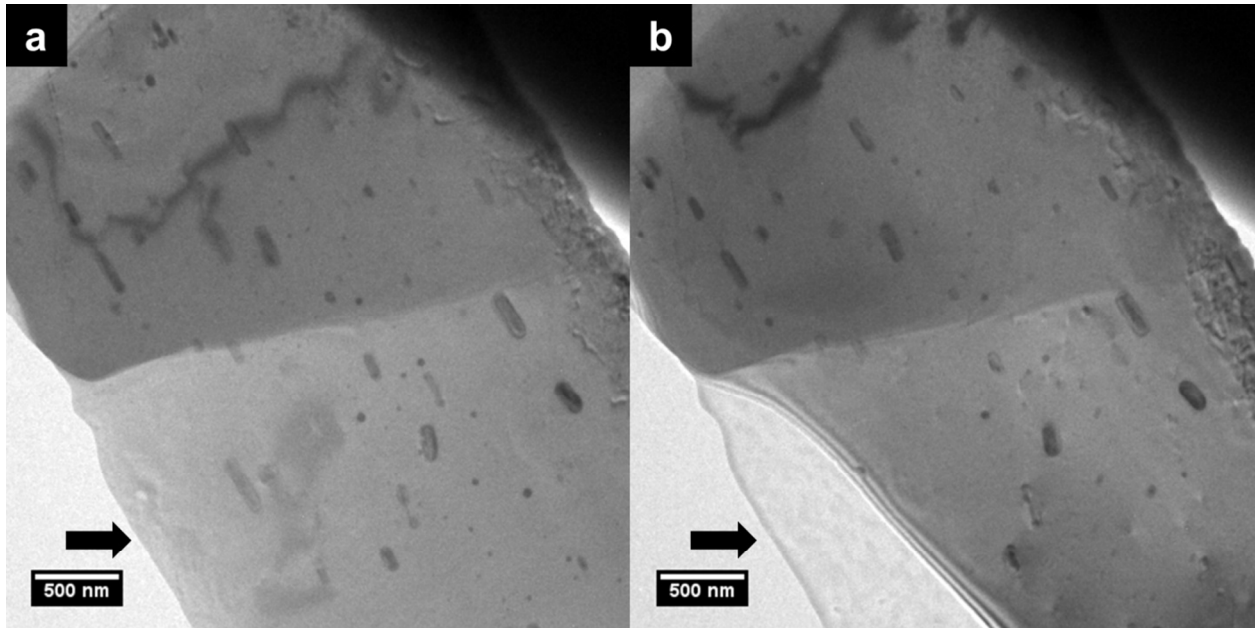


**Figure S10.** Bright-field TEM images of an AA2024 specimen **(a)** just when the temperature is raised to 450°C and **(b)** 10 seconds after the temperature reaches 450°C, shows the large surface diffusion from the edge of the specimen as indicated by the arrow. Note that surface contamination/oxide remains behind.

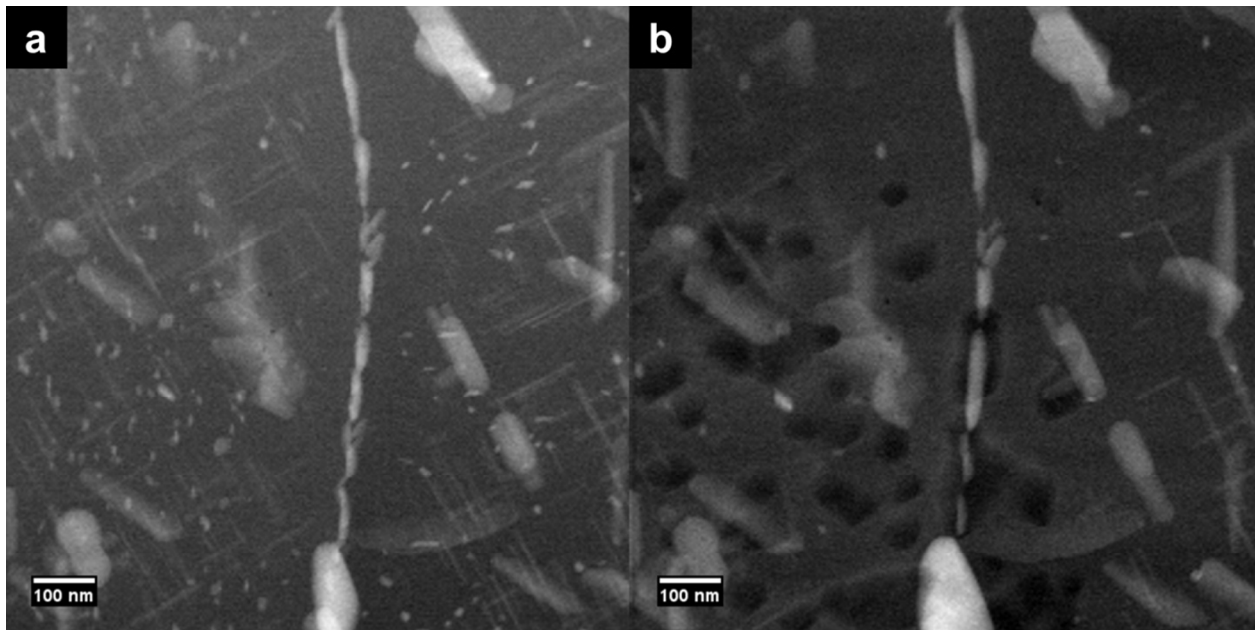


**Figure S11.** STEM-ADF images using a probe current of **(a)**  $\sim 0.3$  nA, the usual probe current for EDX maps in this study with a frame time of 100 s for an area of  $512 \times 512$  pixels<sup>2</sup> and **(b)**  $\sim 3$  nA to improve the acquisition times. At higher probe currents, significant specimen damage, formation of holes that show up as dark areas in the square, is observed.

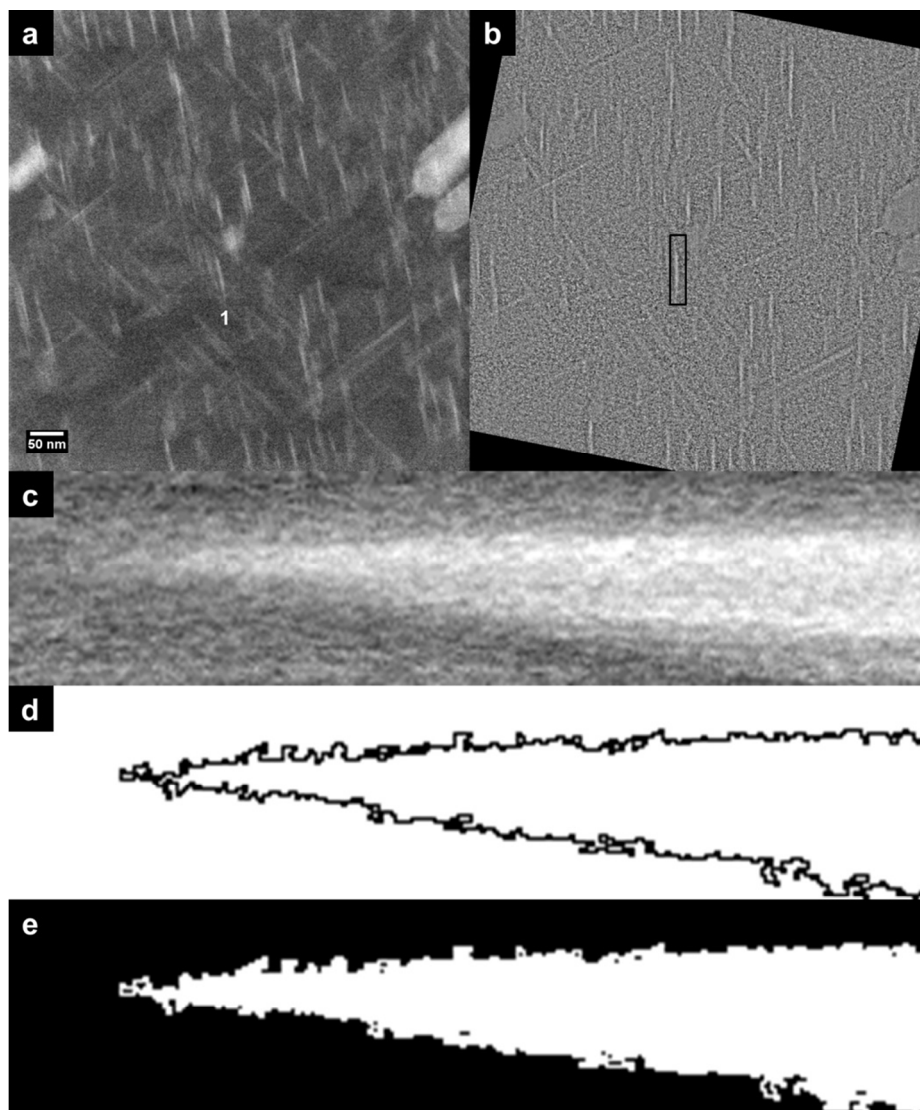


**Figure S12.** (a) Snapshot obtained from the end of an STEM-ADF movie (Supplementary Movie S3). (b) Final frame of the same movie after applying a Gaussian blur and rotating the image to make one family of precipitates vertical. (c) Orthogonal view, YZ (length-time) projection shows the contrast variation from the image stack due to the increase in the precipitate length marked by a rectangle in (b). (d) Outline map of (c) generated by setting appropriate thresholds. (e) Bitmap image where all the pixels outside the outline are set to 0 and inside to 1. From (e), the summation of pixels along the  $y$ -axis now gives the change in length of precipitate with time.

**Supplementary Table S1.** Calculated diffusion coefficients and diffusion lengths for various solute elements in Al; valid for the very dilute limit. The impurity diffusion coefficient is defined as  $D=D_0 \exp[-Q/RT]$ , from which the diffusion length can be calculated as  $L=2\sqrt{(Dt)}$ . Values for the pre-exponential coefficient  $D_0$  and the activation energy  $Q$  are taken from the literature <sup>6</sup>.  $R$  is the gas constant and  $T$  the absolute temperature. For calculation of the diffusion lengths, we used a time period of  $t=900$  s.

Solute element	$D_0$ (m <sup>2</sup> /s)	$Q$ (kJ/mole)	Diffusivity $D(T)$ (m <sup>2</sup> /s)						
			$T(^{\circ}\text{C})$	20	100	200	250	300	400
			$T(\text{K})$	293	373	473	523	573	673
Cu	4.44E-05	133.9		6.0E-29	7.9E-24	7.3E-20	1.9E-18	2.8E-17	1.8E-15
Mg	1.49E-05	120.5		4.9E-27	2.0E-22	7.4E-19	1.4E-17	1.5E-16	6.6E-15
Mn	1.35E-02	211.5		2.7E-40	3.3E-32	5.9E-26	1.0E-23	7.1E-22	5.2E-19
Si	1.38E-05	117.6		1.5E-26	4.7E-22	1.4E-18	2.5E-17	2.6E-16	1.0E-14

## REFERENCES

1. Khan, I. N.; Starink, M. J.; Yan, J. L. *Materials Science and Engineering: A* **2008**, 472, (1–2), 66-74.
2. Batenburg, K. J.; Bals, S.; Sijbers, J.; Kübel, C.; Midgley, P. A.; Hernandez, J. C.; Kaiser, U.; Encina, E. R.; Coronado, E. A.; Van Tendeloo, G. *Ultramicroscopy* **2009**, 109, (6), 730-740.
3. Ferrante, M.; Doherty, R. D. *Acta Metallurgica* **1979**, 27, (10), 1603-1614.
4. Wang, S. B.; Chen, J. H.; Yin, M. J.; Liu, Z. R.; Yuan, D. W.; Liu, J. Z.; Liu, C. H.; Wu, C. L. *Acta Materialia* **2012**, 60, (19), 6573-6580.
5. Schindelin, J.; Arganda-Carreras, I.; Frise, E.; Kaynig, V.; Longair, M.; Pietzsch, T.; Preibisch, S.; Rueden, C.; Saalfeld, S.; Schmid, B.; Tinevez, J.-Y.; White, D. J.; Hartenstein, V.; Eliceiri, K.; Tomancak, P.; Cardona, A. *Nature Methods* **2012**, 9, (7), 676-682.
6. Du, Y.; Chang, Y. A.; Huang, B.; Gong, W.; Jin, Z.; Xu, H.; Yuan, Z.; Liu, Y.; He, Y.; Xie, F. Y. *Materials Science and Engineering: A* **2003**, 363, (1–2), 140-151.